SCIENCE CHINA
Physics, Mechanics & Astronomy

• Article •

March 2023 Vol. 66 No. 3: 232011
https://doi.org/10.1007/s11433-022-2041-8

Effects of a phase transition on two-pion interferometry in heavy ion collisions at $\sqrt{s_{\rm NN}}$ = 2.4-7.7 GeV

Pengcheng Li[1,2,3], Jan Steinheimer[4], Tom Reichert[1,6], Apiwit Kittiratpattana[1,7], Marcus Bleicher[1,5,6], and Qingfeng Li[2*]

[1] *Institut für Theoretische Physik, Johann Wolfgang Goethe Universität Frankfurt, Frankfurt am Main 60438, Germany;*
[2] *School of Science, Huzhou University, Huzhou 313000, China;*
[3] *School of Nuclear Science and Technology, Lanzhou University, Lanzhou 730000, China;*
[4] *Frankfurt Institute for Advanced Studies, Frankfurt am Main 60438, Germany;*
[5] *GSI Helmholtzzentrum fürSchwerionenforschung GmbH, Darmstadt 64291, Germany;*
[6] *Helmholtz Research Academy Hesse for FAIR (HFHF), GSI Helmholtz Center for Heavy Ion Physics, Campus Frankfurt, Frankfurt am Main 60438, Germany;*
[7] *Center of Excellence in High Energy Physics & Astrophysics, School of Physics, Suranaree University of Technology, Nakhon Ratchasima 30000, Thailand*

Received September 20, 2022; accepted November 17, 2022; published online December 19, 2022

Hanbury-Brown-Twiss (HBT) correlations for charged pions in central Au+Au collisions at $\sqrt{s_{\rm NN}}$ = 2.4-7.7 GeV (corresponding to beam kinetic energies in the fixed target frame from $E_{\rm lab}$ = 1.23 to 30 GeV/nucleon) are calculated using the ultra-relativistic quantum molecular dynamics model with different equations of state (EoSs). The effects of a phase transition at high baryon densities are clearly observed in the explored HBT parameters. The results show that the available data on the HBT radii, $R_{\rm O}/R_{\rm S}$ and $R_{\rm O}^2 - R_{\rm S}^2$, in the investigated energy region favor a relatively stiff EoS at low beam energies, which then turns into a soft EoS at high collision energies consistent with astrophysical constraints on the high-density EoS of quantum chromodynamics (QCD). The specific effects of two different phase transition scenarios on $R_{\rm O}/R_{\rm S}$ and $R_{\rm O}^2 - R_{\rm S}^2$ are investigated. A phase transition with a significant softening of the EoS below four times the nuclear saturation density can be excluded using HBT data. Our results highlight that the pion's $R_{\rm O}/R_{\rm S}$ and $R_{\rm O}^2 - R_{\rm S}^2$ are sensitive to the stiffness of the EoS and can be used to constrain and understand the QCD EoS in a high baryon density region.

heavy ion collisions, HBT correlation, equation of state

PACS number(s): 25.75.-q, 25.75.Dw, 25.75.Gz

Citation: P. Li, J. Steinheimer, T. Reichert, A. Kittiratpattana, M. Bleicher, and Q. Li, Effects of a phase transition on two-pion interferometry in heavy ion collisions at $\sqrt{s_{\rm NN}}$ = 2.4-7.7 GeV, Sci. China-Phys. Mech. Astron. **66**, 232011 (2023), https://doi.org/10.1007/s11433-022-2041-8

1 Introduction

The exploration of the properties of hot and dense nuclear matter is among the major goals of today's largest accelerator facilitates. Theoretically, such a matter is described by the theory of strong interaction, called quantum chromodynamics (QCD). To obtain ab-initio results of QCD, one is unfortunately restricted to lattice QCD calculations for static systems at high temperatures and small baryo-chemical potentials (the main reason for this restriction is the so-called sign problem [1]). The current state-of-the-art lattice QCD calculations predict a crossover transition between the

*Corresponding author (email: liqf@zjhu.edu.cn)

hadronic phase and quark-gluon plasma (QGP) phase at a vanishing baryon density at a temperature of $T \simeq 150$ MeV [2,3]. Many model calculations predict that with the increase in the net-baryon density, the phase transition becomes first order and ends at a critical endpoint (CEP) at a finite temperature and density [4-6]. Relativistic heavy ion collisions (HICs) at terrestrial laboratories allow the investigation of the properties of strongly interacting matter in a controlled environment. By changing the mass or centrality of the impinging nuclei and collision energy, one can vary the initially created densities and temperatures, which lead to different freeze-out conditions of baryon chemical potential ($\mu_{\rm B}$) and temperature T after an approximately isentropic expansion [5,7].

To investigate the signatures of a deconfined QGP and search for evidence of a possible first-order phase transition and the location of its CEP, on the experimental side, several experimental programs at GSI, BNL, and CERN have been successfully run. To obtain further data, future facilities such as FAIR, NICA, and HIAF are proposed and currently built. Over the past decades, in the first phase of the Beam Energy Scan program at the Relativistic Heavy Ion Collider (RHIC) (BES-I), Au+Au collision data at $\sqrt{s_{\rm NN}} = 7.7$ to 200 GeV were collected and analyzed. Based on the results from BES-I, the region of interest can be narrowed to collision energies below $\sqrt{s_{\rm NN}} = 20$ GeV [8]. Because the lowest beam energy that is accessible at the RHIC in the collider mode is $\sqrt{s_{\rm NN}} = 7.7$ GeV, a fixed-target (FXT) program has been developed to allow the STAR experiment to access energies from $\sqrt{s_{\rm NN}} = 3.0$ to 7.7 GeV [9].

In addition to this large body of (upcoming) experimental data, there have been substantial developments on the theoretical and modeling side. As an important tool to extract information on the nuclear equation of state (EoS) and the properties of hadrons from low- to relativistic-energy HICs, transport theories have been used for many years. To establish a theoretical systematic error and disentangle the causes that lead to different predictions, various comparisons of different transport models have been performed over the years [10-14]. Moreover, many hydrodynamic approaches and hybrid models, which incorporate different EoSs, have been widely used to understand the properties of dense strongly interacting matters at ultra-relativistic beam energies [15-21]. Various observables have been suggested to explore the locations of first-order quark-hadron phase transition boundary and CEP, such as high-order cumulants [22-24], intermittency analysis [25], the yield ratio of light nuclei [26], and Hanbury-Brown-Twiss (HBT) interferometry [27] (see refs. [5, 28] for an overview and references therein).

In this work, we mainly focus on the pion intensity interferometry (HBT interferometry) [29, 30], which can be used to reveal the space-time substructure and momentum correlations of the freeze-out configuration in HICs. For a detailed description of the history and development of HBT interferometry, the reader is referred to refs. [29-40]. One can usually extract the HBT radii (source radii), which can characterize the size of regions of homogeneity in the kinetic freeze-out volume, from two-particle correlation functions. The two-particle correlation functions, which are constructed from the emission sources by the HBT technique, will be influenced by the EoS [41]. Moreover, the HBT radii parameters are sensitive to a first-order phase transition and may reveal the CEP in the QCD phase diagram [39,42-44]. Based on the prediction, a non-monotonic behavior (maximum) in the excitation functions for the emission source radii ratio and difference obtained from two pion interferometry measurements in Au+Au collisions would serve as a signal for a phase transition.

Such behavior was observed by the STAR experiment [27,36], but at a very high beam energy of $\sqrt{s_{\rm NN}} \approx 20$ GeV. Thus, the investigations about the effects of the EoS on the HBT interferometry within different models are mostly restricted to high energies [44-47]. Because other observables, such as fluctuations did not show the behavior expected from a phase transition at such high beam energies, the interpretation is still in question.

To approach this challenge, it is important to develop models that can not only predict single observables but also predict a wide range of observables in a consistent way that allows a direct comparison with experiments. A previous work [48] showed how any density-dependent EoS can be implemented in the microscopic transport model ultra-relativistic quantum molecular dynamics (UrQMD). This now offers the opportunity to implement different phase transition scenarios in a consistent way and study a variety of possible observables. Ultimately, this will allow us to make consistent statements on the existence of a phase transition and its possible location. The effects of a phase transition on hadronic flow observables have already been shown to be significant in this implementation of the UrQMD model [49]. We also expect that the density-dependent potentials will make a sizable contribution to the proton and net-charge number fluctuations [50,51] during a collision.

Thus, it is interesting and necessary to explore the influence of the EoS on the pion interferometry in HICs at several GeV beam energies within the same framework to make predictions on concerted signals for the phase transition from different measurements.

This paper is organized as follows. In sect. 2, the UrQMD model and methods are briefly described. In sect. 3, the three-dimensional pion HBT radius results are shown. Finally, in sect. 4, the conclusions are presented.

2 Model and method

2.1 UrQMD model and EoS

In the present study, we use the current version of the UrQMD transport model (UrQMD 3.5) [13,52,53] to investigate the pion intensity interferometry in HICs. The UrQMD model can be applied in different modes. At high energies, the cascade mode in which the hadrons interact through binary scattering according to a geometrical interpretation of elastic and inelastic cross sections is most often used. At low energies, it is also necessary to incorporate the nuclear interactions for a complete modeling of the transport dynamics (calculation with the nuclear potential). In the mode when nuclear potential interactions are taken into account, each hadron is represented by Gaussian wave packets with a certain width, and after the initialization of the projectile and target nuclei, the position and momentum of the i-th hadron is propagated according to Hamilton's equation of motion, which read as: $\dot{\mathbf{r}}_i = \frac{\partial\langle H\rangle}{\partial \mathbf{p}_i}$, $\dot{\mathbf{p}}_i = -\frac{\partial\langle H\rangle}{\partial \mathbf{r}_i}$. Here, $\langle H\rangle$ is the total Hamiltonian function of the system, which consists of the kinetic energies $\sum_i T_i$ and the effective interaction potential energies $\sum_i V_i$ of all baryons i in the system. In the default version of the UrQMD model, the potential energies include the two-body and three-body Skyrme, Yukawa, Coulomb, and Pauli terms [54-58][1)] . The Skyrme potential is computed from the single particle energy as $U(\rho_\mathrm{b}) = \frac{\partial(\rho_\mathrm{b}\cdot V(\rho_\mathrm{b}))}{\partial\rho_\mathrm{b}}$ and can be expressed as $U = \alpha\left(\frac{\rho_\mathrm{b}}{\rho_0}\right)+\beta\left(\frac{\rho_\mathrm{b}}{\rho_0}\right)^\gamma$, where ρ_b is the baryonic interaction density in units of $\rho_0 = 0.16$ fm^{-3}, the ground state baryon density. By changing the parameters α, β, and γ, one can change the stiffness of the EoS (usually termed as a hard or soft EoS for a large or small value of the incompressibility K_0, respectively). In the following, calculations within the cascade mode, representing a hadron resonance gas EoS without potentials [18] and a hard Skyrme EoS (K_0 = 380 MeV) in the molecular dynamics mode will serve as benchmark simulations, because the stiffness of the EoS at high densities is still under debate [59-66].

The pion-nucleon potential in the mean field is not considered in the current work because the pion-nucleon potential in dense nuclear matter is not well understood up to now [67-73]. In our previous work [73], including the pion optical potential based on the perturbation expansion of the Δ-hole model, the comparisons between the model simulations and the experimental data in the centrality, rapidity, transverse momentum, and transverse-velocity dependence of the pion collective flows generally favor a weak pion-nucleon potential.

In addition, several novel EoSs are implemented through effective density-dependent potentials to gain insights into the properties of strongly interacting matter. Here, the EoS is based on a realistic CMF model with different phase transition scenarios, adopted to explore the sensitivity of the pion interferometry to the EoS. This CMF EoS was first incorporated in the UrQMD model in ref. [48], and it was achieved by devising a method by which the mean-field potential energy V that enters the equations of motion can be calculated from the energy per baryon of the CMF model [74], as described in detail in ref. [48]. The CMF model incorporates the main concepts of QCD phenomenology: chiral interactions in the baryon octet, full PDG hadron list, excluded volume repulsive interactions among all hadrons, baryon parity doubling, and quarks coupled to an effective Polyakov loop potential. The CMF model describes many aspects of QCD phenomenology, and has been widely employed as the EoS in the hydrodynamic simulations of HICs and binary neutron star mergers. A detailed description of the CMF model and applications to the exploration of HICs can be found in refs. [19, 48, 74-80]. Further studies have shown how this formalism can be extended to include a phase transition at high densities [49]. This phase transition is characterized by an unstable region, i.e., a range in density at which the isothermal speed of sound becomes imaginary. In addition to the phase transition scenario (PT2), which was already introduced in ref. [49], we now also include a new phase transition scenario PT3, which we will discuss below.

Figure 1(a) shows the effective field energy per baryon calculated from different scenarios of the CMF EoS. A direct comparison to the hard Skyrme potential EoS can be found in ref. [48]. The standard CMF EoS shows a similar behavior in the mean-field potential V as that of the hard Skyrme EoS above saturation up to about four times saturation density (ρ_0) and then softens at even higher densities due to a crossover to the high density limit of a free gas of three quark flavors. All three kinds of CMF EoSs show the same behavior in V and p up to approximately $3\rho_0$.

As it is more instructive to discuss the properties of the EoS in terms of the pressure, Figure 1(b) shows the pressure of the effective EoS as a function of the baryon density. The pressure is calculated by

$$P(\rho_\mathrm{b}, T) = P^\mathrm{id}(\rho_\mathrm{b}, T) + \int_0^{\rho_\mathrm{b}} \rho' \frac{\partial U(\rho')}{\partial \rho'} \mathrm{d}\rho', \tag{1}$$

where $P^\mathrm{id}(\rho_\mathrm{b}, T)$ is the pressure of an ideal Fermi-gas of hadrons and $U(\rho_\mathrm{b})$ is the density-dependent single particle potential [49].

As the density increases, the CMF_PT2 EoS becomes mechanically unstable at 2.5 times the saturation density and

1) The Pauli term is usually turned off, and the Yukawa term is negligible for the beam energies investigated here.

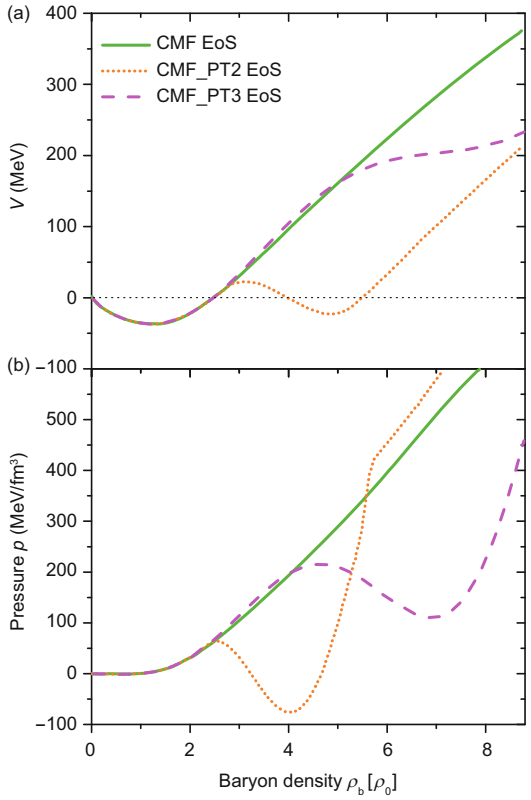

Figure 1 (Color online) Density-dependent potential field energy V (a) and corresponding pressure p (b) shown for the different scenarios used in the chiral mean-field (CMF) EoS. CMF_PT2 and CMF_PT3 include a phase transition and an unstable region at different densities, indicated by the negative slope of the pressure with respect to the density. The default CMF EoS corresponds to a smooth crossover transition.

reaches the minimum pressure at approximately $4\rho_0$. The CMF_PT3 EoS behaves similarly to the standard CMF EoS until approximately $5\rho_0$, above which it then becomes also mechanically unstable due to the phase transition. Hence, in the PT2 case, the transition can be reached already at a rather low density (low collision energies), and the onset of the unstable phase in PT3 is at a density that might be difficult to reach for most collision systems.

2.2 Pion HBT analysis

To explore the effects of various EoSs with and without different phase transitions, we perform UrQMD calculations to obtain the pions' freeze-out phase space coordinates. A freeze-out in UrQMD is defined as the space-time point of the last interaction (either a collision or decay), and the freeze-out times of pions are not necessary to be equal as they should be in the pair rest frame when computing the relative wave function of the $\pi\pi$ pairs. The freeze-out space-time coordinates and four-momentum serve as the input for the "correlation after-burner" (CRAB v3.0β)[2] program, provided by S. Pratt. CRAB constructs the HBT correlation function defined as follows:

$$C(\mathbf{k},\mathbf{q}) = 1 + \frac{\int \mathrm{d}^4x_1\mathrm{d}^4x_2 S(x_1,\mathbf{p}_1)S(x_2,\mathbf{p}_2)|\phi(\mathbf{q},\mathbf{r})|^2}{\int \mathrm{d}^4x_1 S(x_1,\mathbf{p}_1)\int \mathrm{d}^4x_2 S(x_2,\mathbf{p}_2)}. \quad (2)$$

Here, $\mathbf{q} = \mathbf{p}_1 - \mathbf{p}_2$ and $\mathbf{k} = (\mathbf{p}_1 + \mathbf{p}_2)/2$ are the relative momentum and average momentum of the two particles, respectively. $S(x,\mathbf{p})$ represents the probability for emitting a particle with momentum $\mathbf{p}$ from the space-time point $x = (\mathbf{r}, t)$. $\phi(\mathbf{q},\mathbf{r})$ is the relative two-particle wave function with $\mathbf{r}$ being their relative position.

The correlation function is then fitted assuming a three-dimensional Gaussian form in the longitudinally comoving system, which is expressed as:

$$C(q_\mathrm{L},q_\mathrm{O},q_\mathrm{S}) = N[(1-\lambda) + \lambda K_\mathrm{C}(q_\mathrm{inv},R_\mathrm{inv})(1+\exp(-R_\mathrm{L}^2q_\mathrm{L}^2 - R_\mathrm{O}^2q_\mathrm{O}^2 - R_\mathrm{S}^2q_\mathrm{S}^2 - 2R_\mathrm{OL}^2q_\mathrm{O}q_\mathrm{L}))], \quad (3)$$

where N is the overall normalization factor and λ is the incoherence factor and lies between 0 (complete coherence) and 1 (complete incoherence) for bosons in realistic HICs [81]. K_C is the Coulomb correction factor depending on q_inv and R_inv [82-84]. In the present work, to make reliable comparisons between the calculated results and experimental data, the Coulomb final-state interactions are taken into account in the CRAB program and fitting process. $q_\mathrm{inv} = \frac{1}{2}\sqrt{(\boldsymbol{p}_1-\boldsymbol{p}_2)^2-(E_1-E_2)^2}$ is the invariant momentum. The resulting HBT radii are R_L, R_O, and R_S corresponding to the longitudinal (the beam direction), outward (the direction of the transverse component of the pair-relative momentum $\mathbf{k}_\mathrm{T} = (\mathbf{p}_{1\mathrm{T}} + \mathbf{p}_{2\mathrm{T}})/2$, and sideward directions (the direction is defined to be perpendicular to the other two directions), R_OL is the cross-term, and q_i is the pair relative momentum in the i direction, e.g., q_L represents the pair relative momentum in the longitudinal direction. In our previous works [85, 86], the non-Gaussian effects on the HBT radii were investigated. The results show that the non-Gaussian effect is the strongest in the longitudinal direction and weakest in the sideward direction, and the non-Gaussian effect is reduced in all directions of the correlation after considering the mean-field potential. These results indicate that the non-Gaussian effect may have a quantitative effect on the HBT radii, but have a slight influence on the ratio $R_\mathrm{O}/R_\mathrm{S}$.

Figure 2 shows the projections of the calculated correlation functions of the π^- source in the outward (left panel), sideward (middle), and longitudinal (right) directions from the central (0%-10%) Au+Au collisions at $\sqrt{s_\mathrm{NN}}$=4.5 GeV. In the analysis, the hard EoS is adopted, $\pi^-\pi^-$ pairs are

2) https://web.pa.msu.edu/people/pratts/freecodes/crab/home.html.

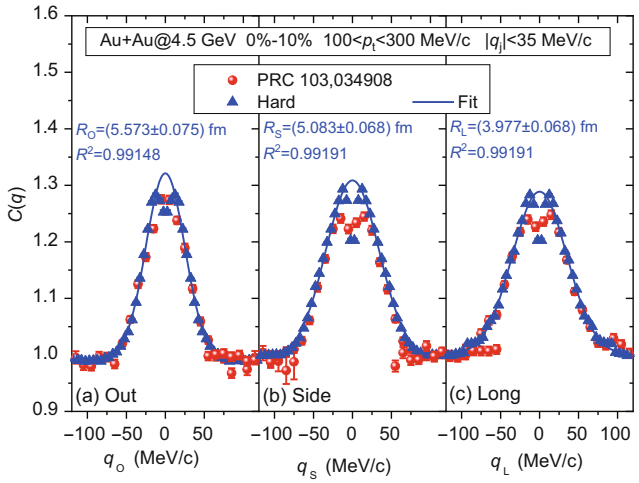

Figure 2 (Color online) Projections of the three-dimensional correlation function (blue triangles) and respective fit (lines). When projecting on one axis, the other two components are restricted to the range ($|q|$ < 35 MeV/c). The experimental data (red circles) are taken from ref. [87].

created from π^- with the momentum 100 < p_T < 300 MeV/c, and the pair transverse momentum 150 < k_T < 600 MeV/c is chosen. For each projection q_i shown, the other components of the relative momentum are integrated over the range $|q_j|$ < 35 MeV/c. The one-dimensional Gaussian fits (lines) ($C(q_i) = N[(1-\lambda)+\lambda K_C(1+\exp(-R_i^2 q_i^2))]$, where i stands for L, O, or S) to the correlation function (points) are also shown with solid lines, separately (the corresponding adjusted R-squared (R^2) and the values of the HBT radius are also given in each plot). The calculated $\pi^-\pi^-$ correlation functions can be reasonably reproduced by the one-dimensional Gaussian fitting. Thus, these reasonable fits can be used to extract radii that characterize the space-time extent of the source.

3 Results and discussions

3.1 Pion freeze-out time and coordinate distributions

To better understand the HBT radii extracted from the HBT interferometry technique, let us investigate the pion freeze-out times and coordinates first.

Figure 3 shows the freeze-out time distribution of the π^- emission in central Au+Au collisions in the inspected energy region. The results from the different EoSs are represented by various colored lines. Pions are mainly frozen out in the time interval 5-25 fm/c, and the pions are frozen out earlier in the case of a harder EoS. In addition, at $\sqrt{s_{NN}}$ = 2.4 GeV (E_{lab} = 1.23 GeV/nucleon), the distributions of the results from all the simulations with potentials are almost identical, and different from the distribution using the cascade mode simply because the EoS for such low densities is very similar for all density-dependent potentials used. As the energy increases, the distributions from the simulations with hard, CMF and CMF_PT3 EoSs remain the same, whereas the distribution from the simulations calculated with CMF_PT2 EoS gradually approaches that of the soft cascade calculations. At $\sqrt{s_{NN}}$ = 7.7 GeV (E_{lab} = 29.7 GeV/nucleon), owing to the CMF and CMF_PT3 EoSs being softer than the hard Skyrme potential and stiffer than the CMF_PT2 EoS, the distributions from the simulations with CMF and CMF_PT3 EoSs lie between the distributions of the simulations with a hard EoS and CMF_PT2 EoS.

The mean values of the π^- freeze-out time (a) and the transverse radii (b) are plotted in Figure 4 shown as different colored lines with symbols. The mean values of the freeze-out time (transverse radii) from hard EoSs are smaller (larger) than those of the softer ones. This general behavior is understood as a result of the large pressure generated by the potentials, leading to a strong expansion, consequently large transverse radii, and an early freeze-out time.

The excitation function of the mean values of the freeze-out time shows a minimum at approximately $\sqrt{s_{NN}}$ = 4 GeV

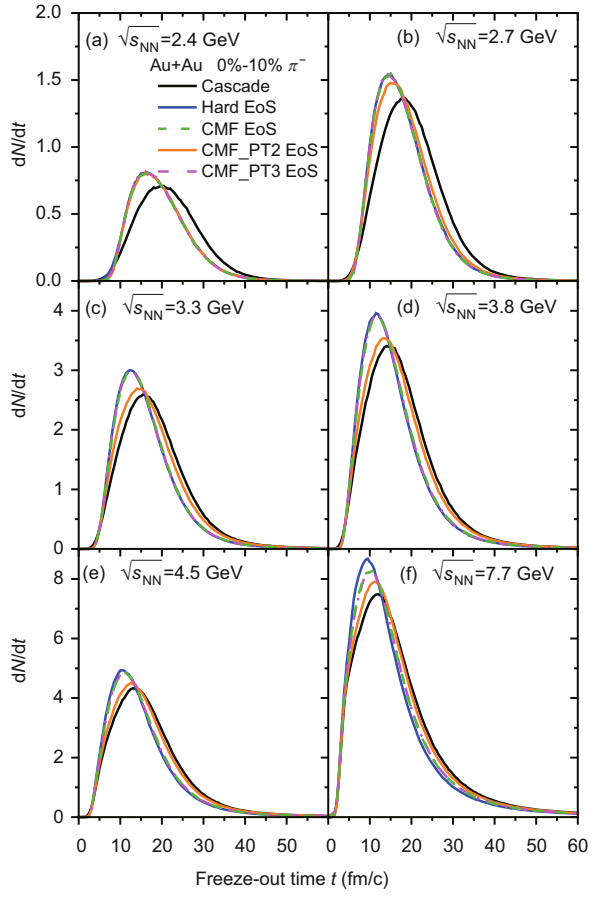

Figure 3 (Color online) Particle production yield as a function of the freeze-out time for π^- from 0% to 10% Au+Au collisions at energies from 2.4 GeV (a) to 7.7 GeV (f). Calculations with the cascade mode are compared with the simulations with potentials.

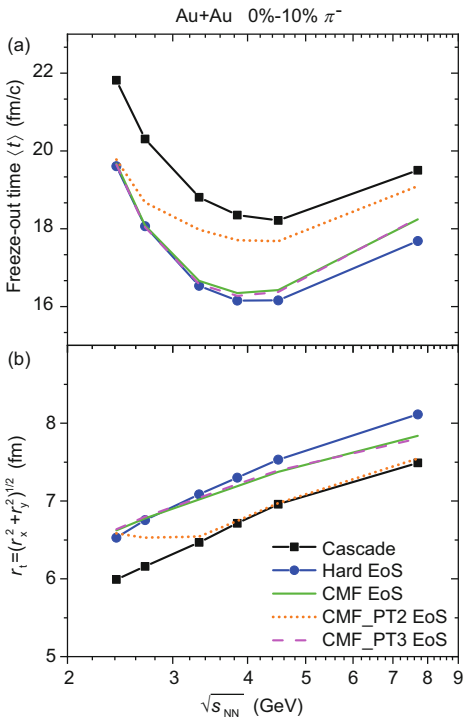

Figure 4 (Color online) (a) Extracted average π^- emission times $\langle t \rangle$ and (b) transverse radii r_t at freeze-out time as a function of collision energies depending on the EoS used.

for all calculations with different EoSs. In addition, a non-trivial energy dependence of the source volume V_f is observed at approximately $\sqrt{s_{NN}}$=4 GeV in experimental data [36, 84, 88]. The minimum observed value in the volume measurement is explained by the change in the particle production mechanism within the UrQMD model [40]. Generally, the particle production in UrQMD either takes place via the decay of a meson or baryon resonance and via string excitation and fragmentation, depending on the invariant mass of the scattering. Up to beam energies of 8-10 GeV/nucleon ($\sqrt{s_{NN}}$ = 3.8-4.7 GeV), the particle production is dominated by resonance decays [40, 52]. In this work, within the UrQMD simulations, the multiplicity ratios between baryons and mesons are independent of the EoS and decrease as the collision energy increases, and $N_{baryon} \approx N_{meson}$ at $\sqrt{s_{NN}} \approx$ 4 GeV. Thus, the minimum observed in the volume measurement and calculated mean freeze-out time could be explained by the change from the baryon-baryon interaction to meson-meson and meson-baryon interactions.

3.2 Effects of the EoS without phase transitions

To set the stage for the investigation of the influence of the different EoSs, we will start with a discussion of the contribution of the Coulomb interaction in the UrQMD model, i.e., the Coulomb interaction before the freeze-out, on HBT observables using the standard hard Skyrme EoS, which also allows describing flow data in this energy regime. The contribution of the Coulomb interaction before freeze-out on the HBT radii of negative pion pairs in Au+Au collisions at $\sqrt{s_{NN}}$ = 2.4 GeV is shown in Figure 5. The simulations without the Coulomb interaction and with only the baryonic contribution to the Coulomb interaction are shown by the dotted black and dashed blue lines, respectively. The simulations with the full Coulomb interaction, also including the meson, are shown by the solid pink lines. The solid stars represent the experimental data taken from ref. [83]. Pair-rapidity is defined as $y_{\pi\pi} = \frac{1}{2}\log\left(\frac{E_1+E_2+p_{l1}+p_{l2}}{E_1+E_2-p_{l1}-p_{l2}}\right)$, with energies E_1 and E_2 and longitudinal momenta p_{l1} and p_{l2} in the center of mass system. Here we employ a cut of $|y_{\pi\pi}| < 0.35$ in line with the data.

First, all three calculations can reproduce the transverse momentum, k_T ($\mathbf{k}_T = (\mathbf{p}_{1T} + \mathbf{p}_{2T})/2$), and dependence of the HBT radii R_L and R_O, except for very small k_T values. The R_S values in the calculations show the values slightly smaller than the experimental data, which in turn makes the ratio R_O/R_S (bottom right) larger than the values obtained from the experimental data. By comparing the results calculated with and without the Coulomb potential, one observes that the effects of the two-body mesonic Coulomb potential during the evolution on the HBT radii and the ratio R_O/R_S are very weak. This is different from flow observables, as was shown in a previous work which indicated that the yield and collective flows of charged pions are indeed influenced by the mesonic Coulomb potential [57]. Such behavior is to be expected because the flow reflects the integrated

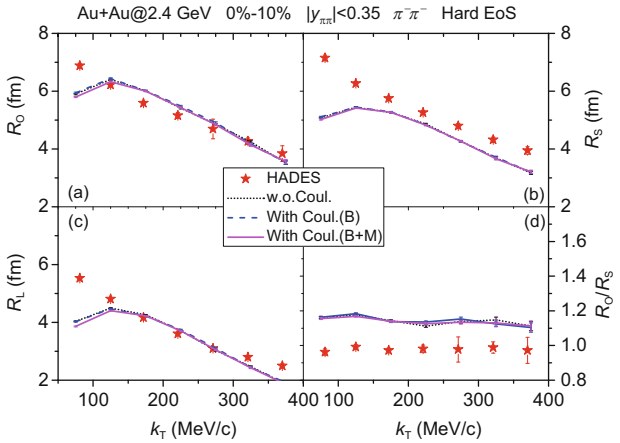

Figure 5 (Color online) k_T dependence of pion HBT radii R_O (a), R_S (b), and R_L (c), and the ratio R_O/R_S (d) of π^- source from the central (0%-10%) Au+Au collisions at $\sqrt{s_{NN}}$ = 2.4 GeV. The results without the Coulomb potential, with the Coulomb potential for baryons only, and with the full Coulomb potential for all hadrons are shown by dotted black, dashed blue, and solid pink lines, separately. The solid stars represent the experimental data taken from ref. [83].

collective motion of single particles, and therefore the Coulomb potential during the system evolution strongly affects the (azimuthal) distribution of the pion emission. Nevertheless, the size of the pion freeze-out source, as seen through the two-pion correlation function in the relative momentum, is only very weakly affected. Therefore, for the following discussion, we will omit the Coulomb effect before a freeze-out on the HBT radii and focus only on the EoS dependence.

Figure 6 shows the calculated k_T dependence of the HBT radii for central (0%-10%) Au+Au collisions at $\sqrt{s_{NN}}$ = 2.4-7.7 GeV. To clarify the influence of nuclear potentials on the pion interferometry, the radii are calculated with and without hadronic potentials (cascade: solid black lines with full squares, hard EoS: solid blue lines with full circles, soft EoS: solid pink lines) and compared with the experimental data [34-36, 83, 84, 87].

With the increasing stiffness of the potential (i.e., strong repulsion as a function of density), R_O at large k_T is driven down while R_S at small k_T is pulled up at low beam energies. This condition results in a decrease in the R_O/R_S ratio as a function of k_T and allows for a better description of the experimental data (shown in Figure 7(a)). This is due to the repulsive nature of the interactions, which reflects the positive potential V at large densities. In addition, the values of the HBT radii and their decrease with k_T can be well reproduced by the calculations with a hard Skyrme potential EoS at low beam energies. The origin of the HBT radii decreases with the increasing transverse momentum has been discussed in many works. We refer interested readers to related works for the details [87, 89-92]. At $\sqrt{s_{NN}}$ = 2.4 GeV, using the soft Skyrme EoS (K_0 = 200 MeV) is added for comparison. Compared with the simulation results with a hard EoS, in simulations with a soft EoS, R_O is increased while R_S is decreased, and the R_O/R_S ratio is increased consequently showcasing the general EoS dependence. Based on the above results, we conclude that a repulsive density-dependent EoS will lead to a stronger phase-space correlation explaining the HBT time-related tensions [93] and leads to a larger emission source.

3.3 Effects of the EoS with phase transitions

A long emission timescale $\Delta\tau$ may arise if the system evolves through a first-order phase transition, which stalls the expansion because the speed of sound vanishes. This should result in a strong increase of R_O compared with R_S [39, 42, 43]. Thus, the difference $R_O^2 - R_S^2$ and ratio R_O/R_S can provide

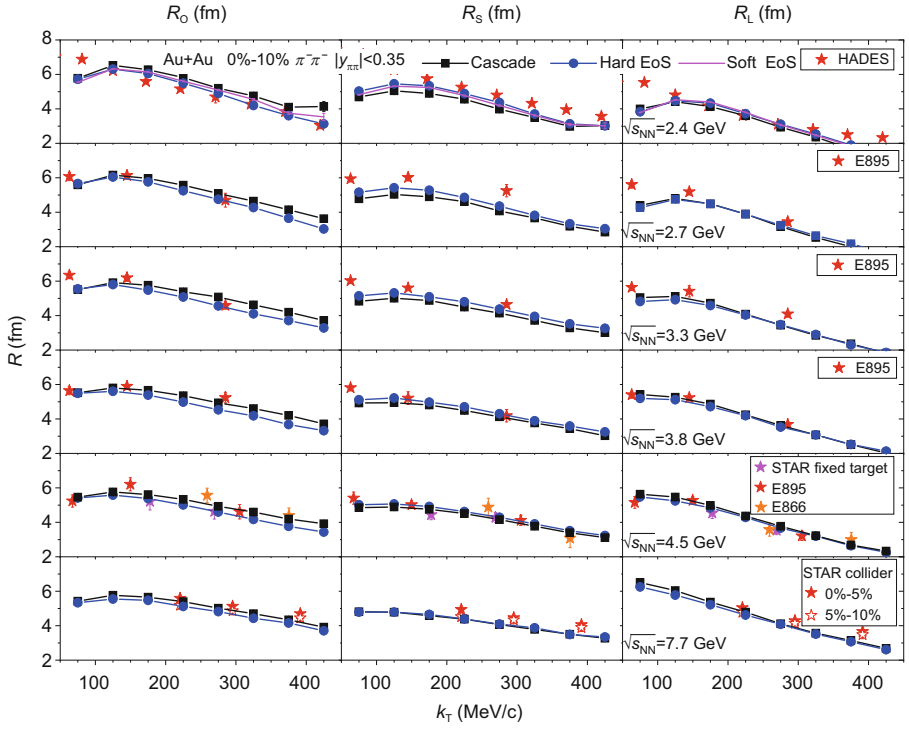

Figure 6 (Color online) Transverse momentum, k_T, dependence of the HBT radii R_O (left panels), R_S (middle panels), and R_L (right panels) for 0%-10% central Au+Au collisions at $\sqrt{s_{NN}}$ = 2.4-7.7 GeV (from top to bottom). The data are indicated by stars, which are obtained by the HADES, E895, E866, and STAR collaborations [34, 36, 84, 87]. The calculations with the cascade mode are shown by lines with black squares, and the calculations with potentials are shown by the blue lines with circles (hard EoS) and the pink lines (soft EoS).

information[3)] on the emission duration, which might be extended if the system undergoes a phase transition.

Experimentally, the situation is, unfortunately, a bit unclear. In the interesting energy region, the experimental data directly taken from refs. [84, 87] have a rather large error bar and supports both interpretations [27, 36, 83]: a local maximum around $\sqrt{s_{\rm NN}} \approx 4$ GeV in the excitation functions of $R_{\rm O}/R_{\rm S}$ and $R_{\rm O}^2 - R_{\rm S}^2$ or a smooth increase. Thus, new experimental and theoretical efforts are needed to clarify the situation, as could be done with the future experiments of CBM at FAIR in Darmstadt and MPD at NICA in Dubna or with the STAR FXT program.

To obtain realistic quantitative predictions for the expected change in the emission time duration due to a phase transition, we employ the UrQMD model with a new EoS including a phase transition. This allows us to directly simulate the effect of a phase transition on $R_{\rm O}/R_{\rm S}$ and $R_{\rm O}^2 - R_{\rm S}^2$ in a consistent manner and pin down the previous qualitative predictions in a quantitatively realistic setup. Figure 7 compares the collision energy dependence of $R_{\rm O}/R_{\rm S}$ (Figure 7(a)) and $R_{\rm O}^2 - R_{\rm S}^2$ (Figure 7(b)) calculated with various EoSs with a broad range of experimental data. By considering the CMF EoS, the ratio $R_{\rm O}/R_{\rm S}$ and square difference $R_{\rm O}^2 - R_{\rm S}^2$ are pulled down in comparison to the cascade mode, and the present data can be qualitatively reproduced. In this energy range, the CMF EoS gives very similar results to the hard Skyrme EoS, which also includes a strong repulsion leading to an earlier pion emission. Generally, the effects of the EoS decrease with increasing collision energy.

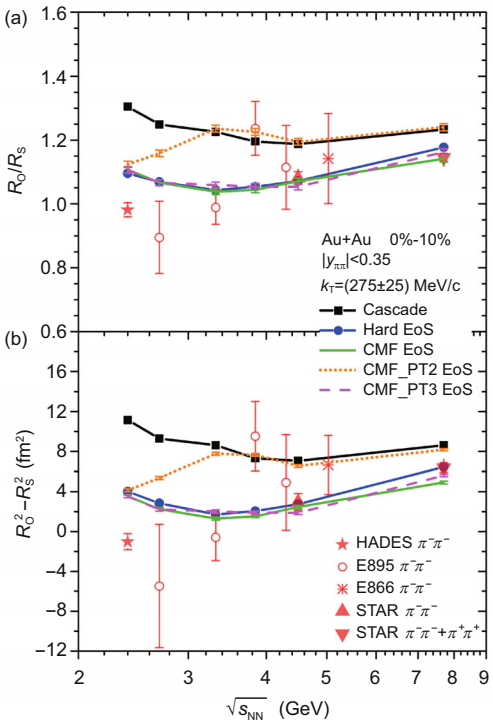

Figure 7 (Color online) Collision energy dependence of the $R_{\rm O}/R_{\rm S}$ (a) and the $R_{\rm O}^2 - R_{\rm S}^2$ (b) extracted from the freeze-out $\pi^-\pi^-$ without and with various EoSs in central Au+Au collisions compared with the experimental data taken from refs. [84, 87].

Here, we turn to the EoS with a phase transition. We compare two CMF EoSs, both including a phase transition. The CMF_PT2 EoS includes a phase transition at low baryon densities, while the CMF_PT3 EoS includes a phase transition at high baryon densities (cf. Figure 1). At the lowest energy ($\sqrt{s_{\rm NN}} = 2.4$ GeV), the results calculated with all CMF EoS are similar as the EoS agrees up to 2.5 times saturation density. As the collision energy increases, the calculated results of the CMF_PT2 EoS gradually increase compared to the standard CMF (or hard/CMF_PT3) EoS as expected for the appearance of a phase transition. Interestingly, they are similar to those with the cascade mode at $\sqrt{s_{\rm NN}} = 3.3$ GeV ($E_{\rm lab} = 4$ GeV/nucleon). This is understood because the pure cascade mode can be considered a super soft EoS and therefore behaves similarly to a phase transition. In addition, the results from the simulations with the hard EoS, CMF EoS, and CMF_PT3 EoS are close to one another in the whole energy region under investigation. In conjunction with Figure 1, the above phenomenon can be well understood. The baryon density of 0%-10% central Au+Au collisions at $\sqrt{s_{\rm NN}} = 2.4$ GeV is less than $3\rho_0$, and the density reaches approximately $5\rho_0$ for 0%-10% central Au+Au collisions at $\sqrt{s_{\rm NN}} = 7.7$ GeV. Thus, the HBT radii calculated with CMF_PT2 are a result of the phase transition encountered for most collision energies, whereas the transition in PT3 is never really reached, even for the highest collision energy. Thus, using CMF_PT3 shows no signal of the phase transition in the explored energy regime. Our results indicate that the pion HBT radii parameters $R_{\rm O}/R_{\rm S}$ and $R_{\rm O}^2 - R_{\rm S}^2$ are very sensitive to the EoS up to densities of 4-5 times saturation density only and are consistent with the absence of any strong softening due to a phase transition up to that point.

4 Conclusions

The UrQMD transport model was used to systematically study the EoS effects on the pion interferometry at collision energies from $\sqrt{s_{\rm NN}} = 2.4$-7.7 GeV. To this aim, UrQMD was supplemented with a novel EoS based on the CMF model, including a phase transition at high baryon densities.

3) Only for a static (non-flowing) source, the emission time can be directly given by $\beta_{\rm t}^2\Delta\tau^2 = R_{\rm O}^2 - R_{\rm S}^2$ [94], where $\beta_{\rm t} = k_{\rm T}/m_{\rm T}$ is the transverse velocity of the emitted pions. For a flowing source, this relationship is unreliable, and extracting timescales from $R_{\rm O}^2 - R_{\rm S}^2$ becomes model dependent [34-36].

The HBT radii and time-related ratio R_O/R_S are weakly affected by the Coulomb potentials during the evolution of the system. However, the source radii parameters (R_O/R_S and $R_O^2 - R_S^2$) are sensitive to the EoS at densities up to 4-5 times nuclear saturation density. In the investigated energy region, the present experimental data can be qualitatively and quantitatively reproduced by simulations with an EoS that shows a stiff behaviour up to four times saturation density and a consecutive softening.

By comparing the available HBT data, we can exclude the existence of a strong phase transition for densities up to 4-5 times saturation density. The present study enables us to directly relate phase transition effects from the pion HBT to, e.g., flow observables predicted within the same approach [49]. Only in this way, can one obtain a consistent picture of the high density EoS of QCD from comparisons with experimental data.

Generally, the effects of the density-dependent EoS on the HBT radii are shown to decrease with increasing collision energy, so statements for higher densities are yet unreliable.

However, in the most interesting energy region, the experimental data still show substantial errors. To elucidate the details of the EoS with HBT data, more theoretical works on understanding the uncertainty from the model are needed on the one hand, and highly accurate experimental data are desired on the other hand.

This work was supported by the National Natural Science Foundation of China (Grant Nos. 11875125, and 12075085). P. Li gratefully acknowledges the financial support from China Scholarship Council (Grant No. 202106180053). J. Steinheimer thanks the Samson AG for funding. The authors are grateful to the C3S2 computing center in Huzhou University for calculation support.

1 A. Pandav, D. Mallick, and B. Mohanty, Prog. Part. Nucl. Phys. **125**, 103960 (2022), arXiv: 2203.07817.
2 Y. Aoki, G. Endrodi, Z. Fodor, S. D. Katz, and K. K. Szabó, Nature **443**, 675 (2006), arXiv: hep-lat/0611014.
3 A. Bazavov, et al. (HotQCD Collaboration), Phys. Rev. D **85**, 054503 (2012), arXiv: 1111.1710.
4 P. Braun-Munzinger, V. Koch, T. Schäfer, and J. Stachel, Phys. Rep. **621**, 76 (2016), arXiv: 1510.00442.
5 A. Bzdak, S. I. Esumi, V. Koch, J. Liao, M. Stephanov, and N. Xu, Phys. Rep. **853**, 1 (2020).
6 P. J. Gunkel, and C. S. Fischer, Phys. Rev. D **104**, 054022 (2021), arXiv: 2106.08356.
7 L. M. Lü, H. Yi, Z. G. Xiao, M. Shao, S. Zhang, G. Q. Xiao, and N. Xu, Sci. China-Phys. Mech. Astron. **60**, 012021 (2017).
8 The STAR Collaboration, *SN0598: Studying the phase diagram of QCD matter at RHIC* (STAR Notes, 2014).
9 K. H. Ackermann, Nucl. Instrum. Methods Phys. Res. Sect. A **499**, 624 (2003).
10 E. L. Bratkovskaya, M. Bleicher, M. Reiter, S. Soff, H. Stöcker, M. van Leeuwen, S. A. Bass, and W. Cassing, Phys. Rev. C **69**, 054907 (2004), arXiv: nucl-th/0402026.
11 E. L. Bratkovskaya, J. Aichelin, M. Thomere, S. Vogel, and M. Bleicher, Phys. Rev. C **87**, 064907 (2013), arXiv: 1301.0786.
12 T. Reichert, A. Elz, T. Song, G. Coci, M. Winn, E. Bratkovskaya, J. Aichelin, J. Steinheimer, and M. Bleicher, J. Phys. G-Nucl. Part. Phys. **49**, 055108 (2022), arXiv: 2111.07652.
13 M. Bleicher, and E. Bratkovskaya, Prog. Part. Nucl. Phys. **122**, 103920 (2022).
14 H. Wolter, et al. (TMEP Collaboration), Prog. Part. Nucl. Phys. **125**, 103962 (2022), arXiv: 2202.06672.
15 S. A. Bass, A. Dumitru, M. Bleicher, L. Bravina, E. Zabrodin, H. Stöcker, and W. Greiner, Phys. Rev. C **60**, 021902 (1999), arXiv: nucl-th/9902062.
16 A. Dumitru, S. A. Bass, M. Bleicher, H. Stöcker, and W. Greiner, Phys. Lett. B **460**, 411 (1999).
17 J. Steinheimer, M. Bleicher, H. Petersen, S. Schramm, H. Stöcker, and D. Zschiesche, Phys. Rev. C **77**, 034901 (2008), arXiv: 0710.0332.
18 H. Petersen, J. Steinheimer, G. Burau, M. Bleicher, and H. Stöcker, Phys. Rev. C **78**, 044901 (2008), arXiv: 0806.1695.
19 J. Steinheimer, S. Schramm, and H. Stöcker, Phys. Rev. C **84**, 045208 (2011), arXiv: 1108.2596.
20 S. W. Lan, and S. S. Shi, Nucl. Sci. Tech. **33**, 21 (2022).
21 C. Shen, and L. Yan, Nucl. Sci. Tech. **31**, 122 (2020).
22 J. Adam, et al. (STAR Collaboration), Phys. Rev. Lett. **126**, 092301 (2021), arXiv: 2001.02852.
23 M. S. Abdallah, et al. (STAR Collaboration), Phys. Rev. Lett. **128**, 202303 (2022), arXiv: 2112.00240.
24 X. H. Jin, J. H. Chen, Z. W. Lin, G. L. Ma, Y. G. Ma, and S. Zhang, Sci. China-Phys. Mech. Astron. **62**, 011012 (2019).
25 T. Anticic, et al. (NA49 Collaboration), Eur. Phys. J. C **75**, 587 (2015).
26 K. J. Sun, L. W. Chen, C. M. Ko, J. Pu, and Z. Xu, Phys. Lett. B **781**, 499 (2018), arXiv: 1801.09382.
27 R. A. Lacey, Phys. Rev. Lett. **114**, 142301 (2015), arXiv: 1411.7931.
28 M. Bluhm, A. Kalweit, M. Nahrgang, M. Arslandok, P. Braun-Munzinger, S. Floerchinger, E. S. Fraga, M. Gazdzicki, C. Hartnack, C. Herold, R. Holzmann, I. Karpenko, M. Kitazawa, V. Koch, S. Leupold, A. Mazeliauskas, B. Mohanty, A. Ohlson, D. Oliinychenko, J. M. Pawlowski, C. Plumberg, G. W. Ridgway, T. Schäfer, I. Selyuzhenkov, J. Stachel, M. Stephanov, D. Teaney, N. Touroux, V. Vovchenko, and N. Wink, Nucl. Phys. A **1003**, 122016 (2020), arXiv: 2001.08831.
29 R. H. Brown, and R. G. Twiss, London Edinburgh Dublin Philos. Mag. J. Sci. **45**, 663 (1954).
30 R. Hanbury Brown, and R. Q. Twiss, Nature **178**, 1046 (1956).
31 G. Goldhaber, S. Goldhaber, W. Lee, and A. Pais, Phys. Rev. **120**, 300 (1960).
32 W. A. Zajc, J. A. Bistirlich, R. R. Bossingham, H. R. Bowman, C. W. Clawson, K. M. Crowe, K. A. Frankel, J. G. Ingersoll, J. M. Kurck, C. J. Martoff, D. L. Murphy, J. O. Rasmussen, J. P. Sullivan, E. Yoo, O. Hashimoto, M. Koike, W. J. McDonald, J. P. Miller, and P. Truöl, Phys. Rev. C **29**, 2173 (1984).
33 S. Pratt, Phys. Rev. Lett. **53**, 1219 (1984).
34 M. A. Lisa, et al. (E895 Collaboration), Phys. Rev. Lett. **84**, 2798 (2000).
35 M. Annan Lisa, S. Pratt, R. Soltz, and U. Wiedemann, Annu. Rev. Nucl. Part. Sci. **55**, 357 (2005), arXiv: nucl-ex/0505014.
36 L. Adamczyk, et al. (STAR Collaboration), Phys. Rev. C **92**, 014904 (2015).
37 Y. J. Wang, F. H. Guan, X. Y. Diao, Q. H. Wu, X. L. Wei, H. R. Yang, P. Ma, Z. Qin, Y. H. Qin, D. Guo, R. J. Hu, L. M. Duan, and Z. G. Xiao, Nucl. Sci. Tech. **32**, 4 (2021).
38 L. Y. Li, P. Ru, and Y. Hu, Nucl. Sci. Tech. **32**, 19 (2021).
39 S. Pratt, Phys. Rev. D **33**, 1314 (1986).
40 Q. Li, C. Shen, and M. Bleicher, Open Phys. **10**, 1131 (2012), arXiv: 1009.3334.
41 Y. G. Ma, Y. B. Wei, W. Q. Shen, X. Z. Cai, J. G. Chen, J. H. Chen, D. Q. Fang, W. Guo, C. W. Ma, G. L. Ma, Q. M. Su, W. D. Tian, K. Wang, T. Z. Yan, C. Zhong, and J. X. Zuo, Phys. Rev. C **73**, 014604 (2006), arXiv: nucl-th/0601078.
42 G. Bertsch, M. Gong, and M. Tohyama, Phys. Rev. C **37**, 1896 (1988).

43 D. H. Rischke, and M. Gyulassy, Nucl. Phys. A **608**, 479 (1996).
44 Q. Li, J. Steinheimer, H. Petersen, M. Bleicher, and H. Stöcker, Phys. Lett. B **674**, 111 (2009), arXiv: 0812.0375.
45 C. J. Zhang, and J. Xu, Phys. Rev. C **96**, 044907 (2017), arXiv: 1707.07272.
46 P. Batyuk, I. Karpenko, R. Lednicky, L. Malinina, K. Mikhaylov, O. Rogachevsky, and D. Wielanek, Phys. Rev. C **96**, 024911 (2017).
47 M. Alqahtani, and M. Strickland, Phys. Rev. C **102**, 064902 (2020), arXiv: 2007.04209.
48 M. Omana Kuttan, A. Motornenko, J. Steinheimer, H. Stoecker, Y. Nara, and M. Bleicher, Eur. Phys. J. C **82**, 427 (2022), arXiv: 2201.01622.
49 J. Steinheimer, A. Motornenko, A. Sorensen, Y. Nara, V. Koch, and M. Bleicher, Eur. Phys. J. C **82**, 911 (2022), arXiv: 2208.12091.
50 J. Steinheimer, Y. Wang, A. Mukherjee, Y. Ye, C. Guo, Q. Li, and H. Stoecker, Phys. Lett. B **785**, 40 (2018), arXiv: 1804.08936.
51 Y. Ye, Y. Wang, Q. Li, D. Lu, and F. Wang, Phys. Rev. C **101**, 034915 (2020), arXiv: 2004.11745.
52 S. Bass, Prog. Part. Nucl. Phys. **41**, 255 (1998).
53 M. Bleicher, E. Zabrodin, C. Spieles, S. A. Bass, C. Ernst, S. Soff, L. Bravina, M. Belkacem, H. Weber, H. Stöcker, and W. Greiner, J. Phys. G-Nucl. Part. Phys. **25**, 1859 (1999), arXiv: hep-ph/9909407.
54 Q. Li, and Z. Li, Mod. Phys. Lett. A **27**, 1250004 (2012), arXiv: 1010.2570.
55 P. Hillmann, J. Steinheimer, and M. Bleicher, J. Phys. G-Nucl. Part. Phys. **45**, 085101 (2018), arXiv: 1802.01951.
56 P. Hillmann, J. Steinheimer, T. Reichert, V. Gaebel, M. Bleicher, S. Sombun, C. Herold, and A. Limphirat, J. Phys. G-Nucl. Part. Phys. **47**, 055101 (2020), arXiv: 1907.04571.
57 Q. Li, Z. Li, S. Soff, M. Bleicher, and H. Stöcker, J. Phys. G-Nucl. Part. Phys. **32**, 151 (2006), arXiv: nucl-th/0509070.
58 Q. F. Li, Y. J. Wang, X. B. Wang, and C. W. Shen, Sci. China-Phys. Mech. Astron. **59**, 632001 (2016), arXiv: 1603.09087.
59 M. S. Abdallah, Phys. Lett. B **827**, 137003 (2022).
60 C. Sturm, et al. (KaoS Collaboration), Phys. Rev. Lett. **86**, 39 (2001), arXiv: nucl-ex/0011001.
61 G. Raaijmakers, S. K. Greif, T. E. Riley, T. Hinderer, K. Hebeler, A. Schwenk, A. L. Watts, S. Nissanke, S. Guillot, J. M. Lattimer, and R. M. Ludlam, Astrophys. J. **893**, L21 (2020), arXiv: 1912.11031.
62 Y. L. Ma, H. K. Lee, W. G. Paeng, and M. Rho, Sci. China-Phys. Mech. Astron. **62**, 112011 (2019), arXiv: 1804.00305.
63 W. C. Yang, Y. L. Ma, and Y. L. Wu, Sci. China-Phys. Mech. Astron. **64**, 252011 (2021), arXiv: 2011.03665.
64 J. Liu, C. Gao, N. Wan, and C. Xu, Nucl. Sci. Tech. **32**, 117 (2021).
65 F. Zhang, and J. Su, Nucl. Sci. Tech. **31**, 77 (2020).
66 G. F. Wei, Q. J. Zhi, X. W. Cao, and Z. W. Long, Nucl. Sci. Tech. **31**, 71 (2020).
67 J. Hong, and P. Danielewicz, Phys. Rev. C **90**, 024605 (2014), arXiv: 1307.7654.
68 Z. Q. Feng, Phys. Rev. C **94**, 054617 (2016), arXiv: 1611.08495.
69 J. Xu, L. W. Chen, C. M. Ko, B. A. Li, and Y. G. Ma, Phys. Rev. C **87**, 067601 (2013), arXiv: 1305.0091.
70 Z. Zhang, and C. M. Ko, Phys. Rev. C **95**, 064604 (2017), arXiv: 1701.06682.
71 C. Fuchs, L. Sehn, E. Lehmann, J. Zipprich, and A. Faessler, Phys. Rev. C **55**, 411 (1997), arXiv: nucl-th/9610027.
72 W. J. Xie, J. Su, L. Zhu, and F. S. Zhang, Phys. Rev. C **97**, 064608 (2018).
73 Y. Liu, Y. Wang, Q. Li, and L. Liu, Phys. Rev. C **97**, 034602 (2018), arXiv: 1804.04295.
74 A. Motornenko, J. Steinheimer, V. Vovchenko, S. Schramm, and H. Stoecker, Phys. Rev. C **101**, 034904 (2020), arXiv: 1905.00866.
75 J. Steinheimer, S. Schramm, and H. Stöcker, J. Phys. G-Nucl. Part. Phys. **38**, 035001 (2011), arXiv: 1009.5239.
76 A. Mukherjee, J. Steinheimer, and S. Schramm, Phys. Rev. C **96**, 025205 (2017), arXiv: 1611.10144.
77 A. Motornenko, S. Pal, A. Bhattacharyya, J. Steinheimer, and H. Stoecker, Phys. Rev. C **103**, 054908 (2021), arXiv: 2009.10848.
78 P. Jakobus, B. Müller, A. Heger, A. Motornenko, J. Steinheimer, and H. Stoecker, Mon. Not. R. Astron. Soc. **516**, 2554 (2022), arXiv: 2204.10397.
79 E. R. Most, A. Motornenko, J. Steinheimer, V. Dexheimer, M. Hanauske, L. Rezzolla, and H. Stoecker, arXiv: 2201.13150.
80 F. Seck, T. Galatyuk, A. Mukherjee, R. Rapp, J. Steinheimer, J. Stroth, and M. Wiest, Phys. Rev. C **106**, 014904 (2022), arXiv: 2010.04614.
81 C. Y. Wong, and W. N. Zhang, Phys. Rev. C **76**, 034905 (2007), arXiv: 0708.1948.
82 Y. M. Sinyukov, R. Lednicky, S. V. Akkelin, J. Pluta, and B. Erazmus, Phys. Lett. B **432**, 248 (1998).
83 J. Adamczewski-Musch, et al. (HADES Collaboration), Phys. Lett. B **795**, 446 (2019), arXiv: 1811.06213.
84 J. Adamczewski-Musch, et al. (HADES Collaboration), Eur. Phys. J. A **56**, 140 (2020), arXiv: 1910.07885.
85 Q. Li, and M. Bleicher, J. Phys. G-Nucl. Part. Phys. **36**, 015111 (2009), arXiv: 0808.3457.
86 Q. Li, G. Gräf, and M. Bleicher, Phys. Rev. C **85**, 034908 (2012), arXiv: 1203.4104.
87 M. S. Abdallah, et al. (STAR Collaboration), Phys. Rev. C **103**, 034908 (2021), arXiv: 2007.14005.
88 Q. Li, M. Bleicher, and H. Stöcker, J. Phys. G-Nucl. Part. Phys. **34**, 2037 (2007), arXiv: 0706.2091.
89 J. Adams, et al. (STAR Collaboration), Phys. Rev. C **71**, 044906 (2005), arXiv: nucl-ex/0411036.
90 Q. Li, M. Bleicher, X. Zhu, and H. Stöcker, J. Phys. G-Nucl. Part. Phys. **34**, 537 (2007).
91 Q. Li, M. Bleicher, and H. Stöcker, Phys. Rev. C **73**, 064908 (2006), arXiv: nucl-th/0602032.
92 L. M. Fang, Y. G. Ma, and S. Zhang, Eur. Phys. J. A **58**, 81 (2022), arXiv: 2205.03988.
93 S. Pratt, Phys. Rev. Lett. **102**, 232301 (2009), arXiv: 0811.3363.
94 U. Heinz, B. Tomášik, U. A. Wiedemann, and Y. F. Wu, Phys. Lett. B **382**, 181 (1996).